RSC Advances

PAPER

View Article Online
View Journal | View Issue

Cite this: *RSC Adv.*, 2021, **11**, 26739

A novel one-step synthesis of Ce/Mn/Fe mixed metal oxide nanocomposites for oxidative removal of hydrogen sulfide at room temperature†

Nishesh Kumar Gupta,[ab] Jiyeol Bae *[ab] and Kwang Soo Kim [ab]

In this study, CeO_2/Fe_2O_3, CeO_2/Mn_2O_3, and $CeO_2/Mn_2O_3/Fe_2O_3$ nanocomposites were synthesized by the calcination of molten salt solutions. The microscopic images confirmed polyhedral nanocrystals of 10–20 nm size, clustered to form nanospheres. The elemental mapping confirmed the uniform distribution of transition metal oxides in the CeO_2 matrix. The X-ray diffraction analysis confirmed the phase purity of metal oxides in nanocomposites. The surface area of nanocomposites was in the range of 16–21 $m^2\ g^{-1}$. X-ray photoelectron spectroscopy confirmed 25–28% of Ce^{3+} ions in the CeO_2 of nanocomposites. These nanocomposites were tested for the removal of hydrogen sulfide gas at room temperature. The maximum adsorption capacity of 28.3 mg g^{-1} was recorded for $CeO_2/Mn_2O_3/Fe_2O_3$ with 500 ppm of H_2S gas and 0.2 L min^{-1} of flow rate. The adsorption mechanism probed by X-ray photoelectron spectroscopy showed the presence of sulfate as the only species formed from the oxidation of H_2S, which was further confirmed by ion chromatography. Thus, the study reports room-temperature oxidation of H_2S over mixed metal composites, which were synthesized by a novel one-step approach.

Received 28th April 2021
Accepted 28th July 2021

DOI: 10.1039/d1ra03309c

rsc.li/rsc-advances

1. Introduction

Hydrogen sulfide (H_2S) is a toxic malodorous gas released from various anthropogenic and natural activities. The energy sector is one of the largest sources of H_2S emission due to its presence in natural gas, tail gas, biogas, and transportation gases like diesel and jet fuels.[1] The H_2S removal is required for clean burning of fuel and prevention of transport pipelines from corrosion and catalysts from poisoning in the gas reforming processes.[1,2] H_2S emitted from these sources are oxidized to SO_2, which further reacts to form acid rain.[3] Thus, the removal of H_2S from sources should be prioritized in the interest of human health and the environment. Adsorption and thermal oxidation approaches are simpler, economical, and environmentally benign methods for the adsorptive/catalytic removal of H_2S from waste gas streams. For adsorptive removal of H_2S, porous adsorbents like activated carbon,[4] modified silica,[5] zeolites,[6] and metal–organic frameworks[7,8] have been reported as efficient materials for the purpose. On the same note, metal oxides could be used as adsorbents at low temperatures and thermal catalysts at elevated temperatures.[9]

Numerous metal oxides as single-phase and composites of Cu, Zn, Mn, Co, Fe, Ni, Ce, Zr, V, and Ti have been studied as thermal catalysts for the oxidative removal of H_2S at elevated temperatures.[9–11] Cerium oxide (CeO_2) is used for different catalytic processes as it has abundant oxygen vacancies and redox properties. Also, CeO_2 is excellent support for transition metal oxides due to superior metal–support interactions.[12,13] More often, CeO_2/transition metal oxide composites are used for the catalytic removal of H_2S at elevated temperatures.[14,15] The same active sites in these metal oxides have been used for H_2S sensing at low temperatures.[16] Thus, it can be safely assumed that these metal oxide composites could be suitable for the catalytic oxidation of H_2S at low temperatures or even at room temperature.

Though room temperature H_2S oxidation studies on CeO_2 or CeO_2-based composites are scarce, several reports on H_2S sensing over these materials are available in the literature.[16,17] Many of the transition metal oxides show excellent H_2S adsorptive/oxidative behaviour at room temperature.[18] Our previous work on the H_2S removal using Mn_2O_3/Fe_2O_3 have demonstrated that even these transition metals could effectively oxidize H_2S to elemental sulfur and sulfates at room temperature.[19] It is interesting to explore CeO_2/transition metal oxides (Mn_2O_3 and Fe_2O_3) as nanocomposites for the room temperature removal of H_2S.

In this work, we have developed nanocomposites of CeO_2 with Mn_2O_3 and Fe_2O_3 by the calcination of molten salt solutions in the air. The synthesized nanocomposites were characterized by various microscopic and spectroscopic techniques.

[a]University of Science and Technology (UST), Daejeon, Republic of Korea
[b]Department of Land, Water, and Environment Research, Korea Institute of Civil Engineering and Building Technology (KICT), Goyang, Republic of Korea. E-mail: baejiyeol@kict.re.kr

† Electronic supplementary information (ESI) available. See DOI: 10.1039/d1ra03309c

Furthermore, the synthesized nanocomposites were tested for the removal of H_2S in ambient conditions. The adsorption mechanism was probed by energy-dispersive X-ray spectroscopy (EDAX), powder X-ray diffraction (PXRD), and X-ray photoelectron spectroscopy (XPS).

2. Materials and methods

2.1. Chemicals

Cerium(III) nitrate hexahydrate ($Ce(NO_3)_3 \cdot 6H_2O$, purity 98.0%), manganese(II) nitrate tetrahydrate ($Mn(NO_3)_2 \cdot 4H_2O$, purity >97.0%), and iron(III) nitrate nonahydrate ($Fe(NO_3)_3 \cdot 9H_2O$, purity 98.5%) were procured from Sigma Aldrich, Germany. H_2S gas (500 ppm balanced with N_2 gas) was purchased from Union Gas, Korea.

2.2. Synthesis of adsorbents

The mixed metal oxides were prepared by the calcination of molten salt solutions in the air. In a typical synthesis process, nitrate salts of Ce, Mn, and Fe (3 : 1 : 1 molar ratio) were mixed in an alumina crucible. The salt mixture was placed in a hot air oven at 70 °C for 24 h to yield a molten salt solution. The molten salt solution was calcined at 700 °C for 24 h to get the desired product. The finely grounded product was named CeMnFe. Likewise, CeMn and CeFe were synthesized by taking Ce : Mn and Ce : Fe in a 3 : 1 molar ratio. Fe_2O_3, Mn_2O_3, and CeO_2 were synthesized using the same protocol from their respective nitrate salts.

2.3. Analytical instruments

The scanning electron microscopy (SEM) images were recorded on a Hitachi S-4300 microscope after coating the samples with a gold–platinum alloy by ion-sputtering (E-1048 Hitachi ion sputter). Transmission electron microscopy (TEM) images were obtained on a JEM-2010F, JEOL, Japan microscope. EDAX analysis was done using X-Maxn 80T, United Kingdom. The nitrogen adsorption–desorption analyses were performed using a Gemini series Micromeritics 2360 instrument at −196 °C after degassing at 400 °C for 6 h. PXRD patterns of mixed metal oxides were recorded on an Ultima IV X-ray diffractometer (Rigajku, Japan) with Cu Kα and Ni filter. The scanning speed was set to 3° min^{-1}. Fourier-Transform Infrared spectroscopy

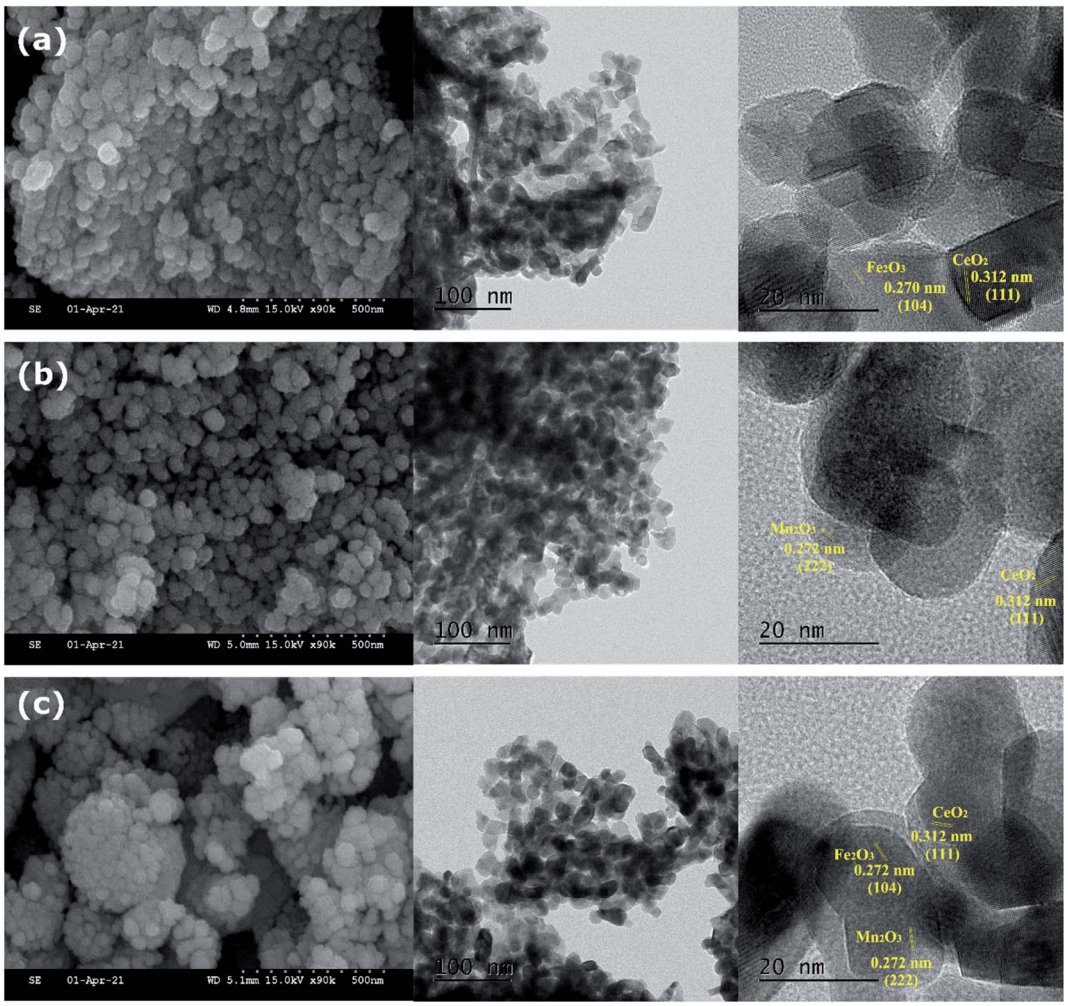

Fig. 1 SEM and TEM images of (a) CeFe; (b) CeMn; (c) CeMnFe.

(FTIR) spectra were obtained on an FTIR spectrometer (Cary 670, Agilent) after pelletization with KBr. XPS analyses were done on a K-alpha XPS instrument (Thermo Scientific Inc., United Kingdom) with a monochromatic Al Kα X-ray source. The pressure was set to 4.8×10^{-9} mbar. Spectra were charge corrected to the main line of the C 1s spectrum (aromatic carbon) set to 284.7 eV. Spectra were analyzed using CasaXPS version 2.3.14. GL(p) = Gaussian/Lorentzian product formula where the mixing is determined by $m = p/100$, GL(100) is a pure Lorentzian while GL(0) is pure Gaussian. GL(30) was used in the present work. The H_2S concentration in effluent gas was analyzed by a GSR-310 multi-gas analyzer (Sensoronic, Korea) with 0.1 ppm as the detection limit. The sulfate in the aqueous phase was quantified by ion chromatography (Thermo Fischer Scientific, AQUION system).

2.4. Adsorption experiment

The breakthrough column studies were performed at room temperature and atmospheric pressure. Exactly 1.0 g of adsorbent was placed in between the glass wool, which was supported on silica beads in a pyrex tube (height: 50 cm, inner diameter: 1 cm).[7] Through it, H_2S gas was passed at a fixed flow rate. The effluent gas was analyzed every 15 s. The effluent concentration of 100 ppm (20%) was considered as the breakthrough point. The effect of moisture was studied by passing moist air (relative humidity ~60%) through the adsorbent bed at a flow rate of 0.2 L min^{-1} for 0.5 h. It was followed by passing H_2S gas at a flow rate of 0.2 L min^{-1}. The effect of air was investigated by blowing atmospheric air at a flow rate of 0.5 L min^{-1} for 1 h, followed by passing H_2S gas at a flow rate of 0.2 L min^{-1}. The spent adsorbent was regenerated by soaking 1.0 g of adsorbent in 20 mL of ammonium hydroxide solution (0.9 mol L^{-1}). After phase separation and drying, the regenerated adsorbent was packed and studied for the next cycle. The adsorption capacity (q, mg g^{-1}) at the breakthrough point was calculated by integration of the area above the breakthrough curve.

$$q = \frac{C_0 Q}{m} \int_0^{t_b} \left(1 - \frac{C}{C_0}\right) dt \quad (1)$$

where C_0 – initial concentration (500 ppm or 0.697 mg L^{-1}), Q – flowrate, m – the mass of adsorbent (g), and t_b – breakthrough time.

3. Results and discussion

3.1. Characterization of adsorbents

The SEM and TEM micrographs of mixed metal oxide nanocomposites are shown in Fig. 1. All three mixed metal oxide nanocomposites have nanospheres clustered together. The HRTEM image at 100 nm resolution showed that the nanospheres were formed with polyhedral nanocrystals of 10–20 nm size. The crystallite planes were assigned by measuring the fringe width in the HRTEM image and correlating it with the inter-planar spacing (d) from the PXRD pattern. The fringe width of 0.312 nm was assigned to the most intense (111) plane of CeO_2,[20] whereas the fringe width of 0.270 nm was assigned to the (104) plane of α-Fe_2O_3.[21] Thus, CeO_2 and Fe_2O_3 nanoparticles were closely present in CeFe (Fig. 1a). In CeMn, the fringe width of 0.270 nm was assigned to the (222) plane of α-Mn_2O_3 (ref. 22; Fig. 1b). For CeMnFe, CeO_2, Fe_2O_3, and Mn_2O_3 nanoparticles were confirmed with their fringe width values (Fig. 1c).

The EDAX line mapping and 2D elemental mapping of mixed metal oxide nanocomposites are shown in Fig. 2 and Fig. S1,† respectively. In CeMn, the Mn density was distributed over the Ce density, which confirmed the deposition of Fe_2O_3 over ceria

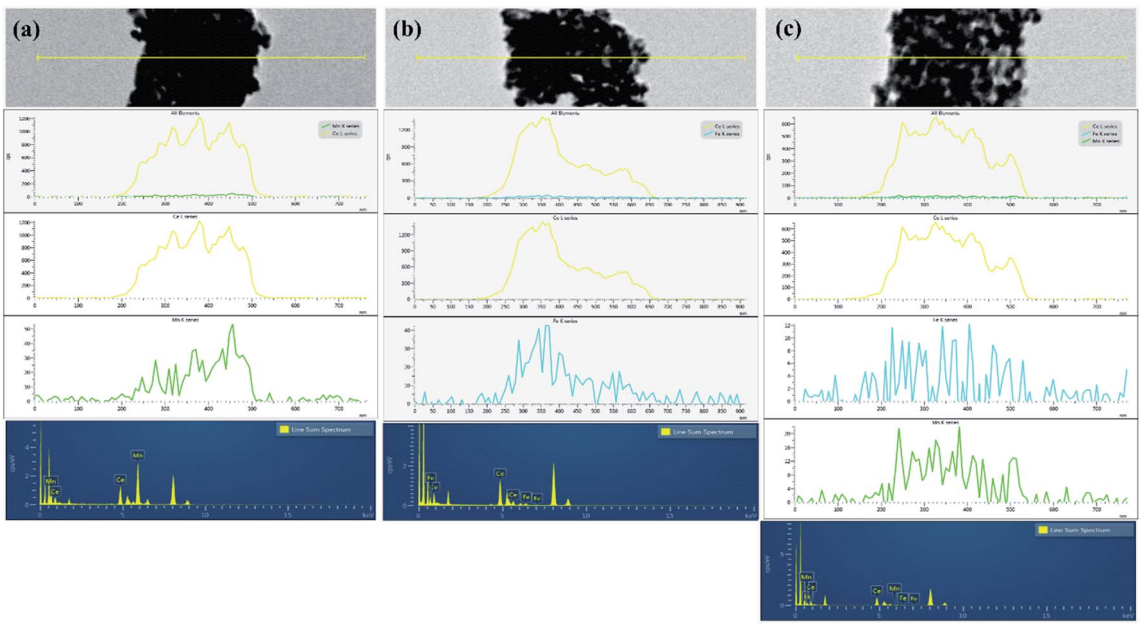

Fig. 2 EDAX line mapping of (a) CeMn; (b) CeFe; (c) CeMnFe.

nanoparticles (Fig. 2a). Moreover, the presence of some N was due to the presence of residual nitrate as nitrate salts were used in the synthesis process (Fig. S1†). For CeFe, besides Ce, O, and N, a uniform presence of Fe was observed (Fig. 2b). In CeMnFe, a uniform presence of Mn and Fe was observed over Ce (Fig. 2c). Thus, the elemental density analysis and line mapping confirmed the uniform distribution of transition metal oxides over CeO_2.

Porosity properties and specific surface area of nanocomposites were calculated from N_2 adsorption–desorption isotherms at −196 °C (Fig. 3a, Fig. S2–S4†). The N_2 isotherms were found identical for all three nanocomposites. The surface area (S_{BET}) of 18.9, 20.6, and 15.6 $m^2\ g^{-1}$ was measured for CeFe, CeMn, and CeMnFe, respectively. The pore volume (V_p), average pore diameter ($D_{p,avg}$), and S_{BET} values are listed in Table 1.

The PXRD patterns of mixed metal oxides are presented in Fig. 3b. The XRD pattern of CeFe has peaks at 28.52°, 33.10°, 47.48°, 56.34°, 59.10°, and 69.50°, which were assigned to the 111, 200, 220, 311, 222, and 400 reflections of CeO_2, respectively (JCPDS file no. 81-0792).[23] Additional peaks at 24.08°, 33.10°, 35.56°, 40.82°, 49.44°, 54.04°, 62.36°, and 63.94° corresponded to the 012, 104, 110, 113, 024, 116, 214, and 300 reflections of α-Fe_2O_3, respectively (JCPDS file no. 75-0033).[21] Other than CeO_2 peaks, additional peaks at 23.14°, 32.96°, 38.24°, 45.18°, 49.34°, 55.18°, and 67.46° for 211, 222, 400, 332, 431, 440, and 622 reflections of α-Mn_2O_3 (JCPDS file no. 24-0508), respectively, were observed in CeMn.[24] For CeMnFe, the peaks corresponding to CeO_2, α-Fe_2O_3, and α-Mn_2O_3 were present.

Table 1 Surface and pore properties of nanocomposites

Adsorbent	S_{BET} ($m^2\ g^{-1}$)	V_p ($cm^3\ g^{-1}$)	$D_{p,avg}$ (nm)
CeFe	18.92	0.096	20.4
CeMn	20.56	0.118	22.9
CeMnFe	15.64	0.094	24.0

The FTIR spectra of mixed metal oxides are shown in Fig. 3c. In the FTIR spectrum of CeFe, the band at 3437 cm^{-1} coupled with a low-intensity band at 1628 cm^{-1} was assigned to the stretching and bending mode of O–H bonds in adsorbed water, respectively.[25] The high-intensity band at 476 and 545 cm^{-1} was assigned to the bending and stretching vibration modes of metal–oxygen bonds, respectively.[21,26] The band at 1052 cm^{-1} was due to the presence of Ce–OH overtone.[23] In CeMn, the bands at 523 and 577 cm^{-1} were assigned to the stretching modes of Ce–O/Mn–O bonds.[27] The band at 678 cm^{-1} was due to the antisymmetric Ce–O–Ce stretching mode of the bridged oxide formed by the condensation of adjacent hydroxyl groups

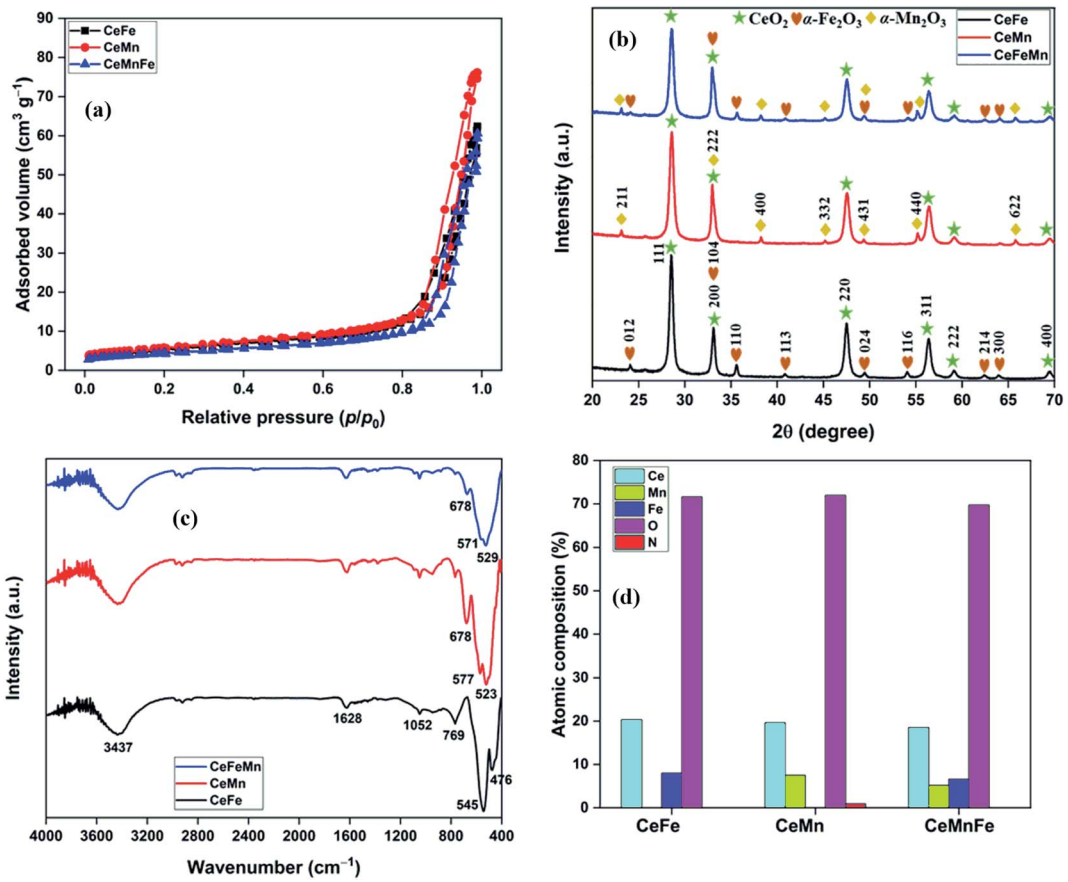

Fig. 3 (a) N_2 adsorption–desorption isotherms; (b) PXRD patterns; (c) FTIR spectra of mixed metal oxides; (d) atomic composition from XPS analysis.

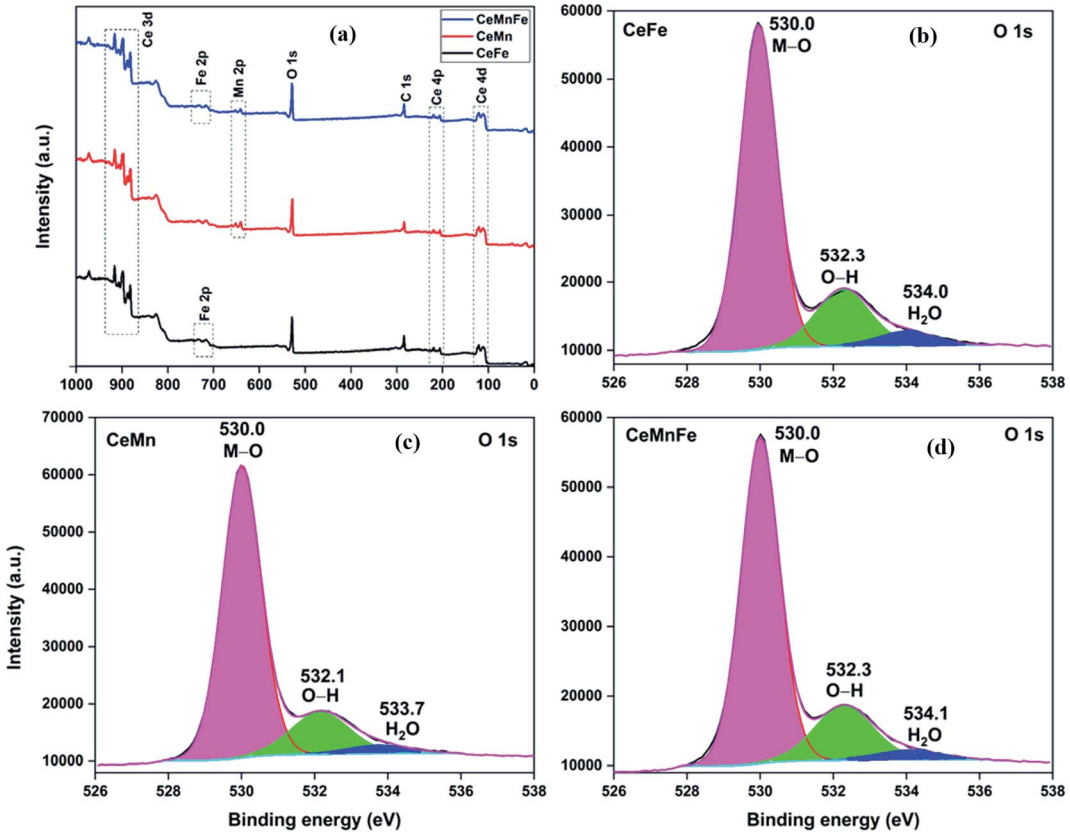

Fig. 4 (a) XPS full scan surveys; HRXPS O 1s spectra of (b) CeFe; (c) CeMn; (d) CeMnFe.

on the surface, similar to Sn–O–Sn stretching.[28] For CeMnFe, the band in 400–700 cm^{-1} was broad, with major bands centred at 529, 571, and 678 cm^{-1} for metal–oxygen stretching vibrations.

The atomic composition obtained from the TEM-EDX analysis validated the molar ratio of metal salts used in the synthesis process (Fig. 3d). The XPS full scan surveys of CeFe, CeMn, and CeMnFe are shown in Fig. 4a. The XPS survey of CeFe has peaks for Ce, C, O, and Fe. The C peak was due to the adventitious carbon. For CeMn, the peak for Mn 2p was present at ~640 eV. For CeMnFe, the peaks corresponding to Ce, Mn, Fe, C, and O were distinctly visible. A small contribution of 0.91% for nitrogen due to the use of nitrate salts in the synthesis process was observed only in CeMn. Overall, the samples were nearly free of nitrogen presence. The HRXPS O 1s spectrum of CeFe has three distinct components at 530.0, 532.3, and 534.0 eV, which were assigned to the lattice oxygen (76.2%), hydroxyl groups (19.1%), and adsorbed water molecules (4.7%), respectively (Fig. 4b, Table 2).[29] For CeMn (Fig. 4c) and CeMnFe

Table 2 The H_2S adsorption capacity of metal oxide adsorbents at room temperature[a]

	Experimental conditions			
Adsorbent	C_0 (ppm)	Flowrate (mL min^{-1})	Breakthrough point (%)	q_e (mg g^{-1})
Mn_3O_4 (ref. 18)	300	—	33.3	16.0[d]
Nanostructured Fe_2O_3 (ref. 38)	200	—	10.0	2.5[d]
Fe_2O_3 pellet[39]	150	810	1.0	3.9[d]
α-Fe_2O_3 powder				24.7[d]
α-Fe_2O_3 (ref. 40)	5000	20	2.6	0.0[d]
Mn_2O_3/Fe_2O_3 (ref. 19)	500	200	80.0	12.0[d]
Cu-exchanged titanosilicate[41]	10	100	5.0	47.0[d]
Fe^{3+}-doped Al-pillared montmorillonite[42]	3000	500	33.3	12.7[w]
CeMnFe [present study]	500	200	20.0	28.3[d]

[a] Superscript letters 'w' and 'd' indicate wet and dry conditions, respectively.

(Fig. 4d), similar contributions were observed for lattice oxygen, O–H, and water molecules (Table S1†).

The HRXPS Ce 3d spectrum of CeFe has peaks at 898.0, 888.7, and 882.0 eV was assigned to the Ce $3d_{5/2}$ profiles. The Ce $3d_{3/2}$ profiles have 916.4, 907.0, and 900.6 eV peaks (Fig. 5a).[30] The Ce $3d_{5/2}$ peaks were fitted to Ce^{3+} (28.1%) and Ce^{4+} (71.9%) oxidation states (Table S2†). For CeMn (Fig. 5b) and CeMnFe (Fig. 5c), similar Ce 3d spectra were observed with 24.1 and 25.5% of Ce^{3+} ions, respectively. The Fe 2p spectra of CeFe and CeMnFe have peaks at 710.0 (Fe $2p_{3/2}$) and 722.6 eV (Fe $2p_{1/2}$) along with two shake-up satellites for Fe^{3+} ions in Fe_2O_3 (Fig. 5d).[31] The Mn 2p spectra of CeMn and CeMnFe have two peaks at 640.0 (Mn $2p_{3/2}$) and 651.9 eV (Mn $2p_{1/2}$) with a spin–orbit splitting of 11.9 eV for Mn^{3+} in Mn_2O_3 (Fig. 5e).[32] The HRXPS N 1s showed a negligible presence of nitrogen on the surface of mixed metal oxides (Fig. 5f).

3.2. Breakthrough studies

The H_2S breakthrough curves of dry metal oxide nanocomposites are shown in Fig. 6a. Among the three nanocomposites, CeMnFe had the adsorption capacity of 12.0 mg g^{-1}, which was higher than that of CeMn (9.5 mg g^{-1}) and CeFe (4.8 mg g^{-1}). Xue *et al.* screened a series of transition metal oxides and their nanocomposites for the adsorptive removal of

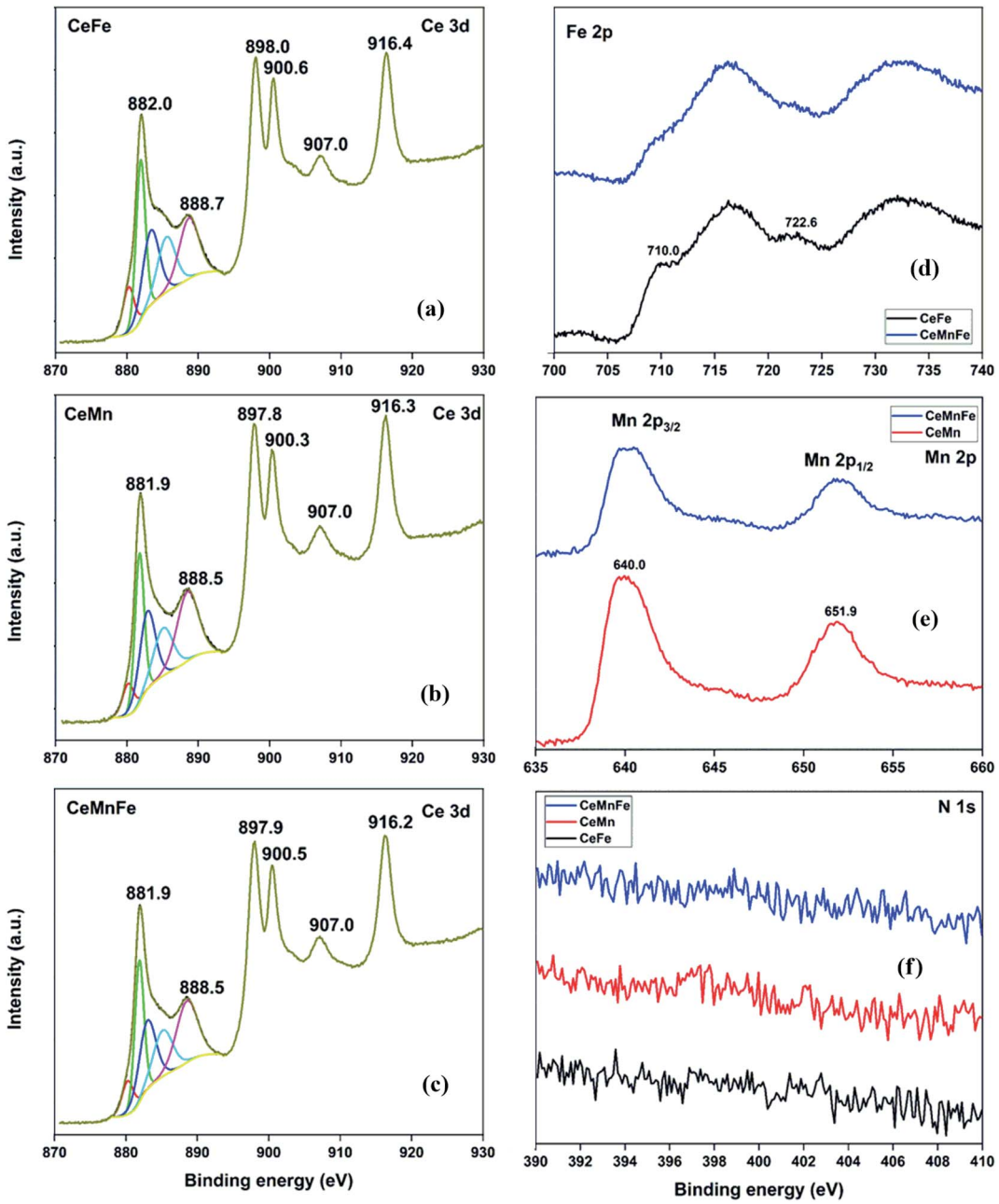

Fig. 5 HRXPS (a–c) Ce 3d; (d) Fe 2p; (e) Mn 2p; (f) N 1s spectra of mixed metal oxides.

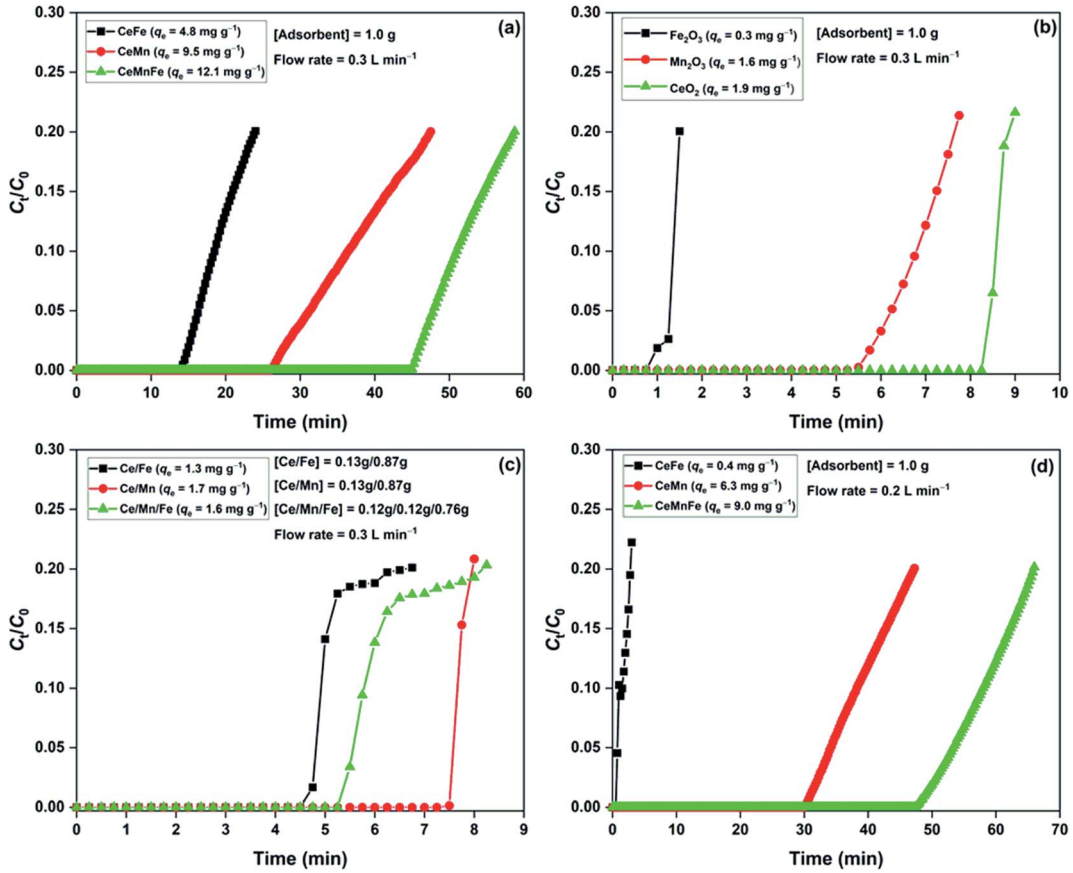

Fig. 6 H_2S breakthrough curves of (a) metal oxide nanocomposites; (b) pure oxides; (c) physically mixed oxides in dry condition; (d) metal oxide nanocomposite in moist condition.

H_2S at room temperature. The study found a higher adsorption capacity of mixed metal oxides compared to binary oxides.[18] For validation, we have presented the adsorption capacity of pure oxides (Fig. 6b) and physical mixture of these oxides (Fig. 6c). The adsorption capacity of Fe_2O_3, Mn_2O_3, and CeO_2 was 0.3, 1.6, and 1.9 mg g^{-1}, respectively. The physically mixed oxides did not show any significant improvement in the H_2S adsorption performance. The adsorption capacity of Ce/Fe (1.3 mg g^{-1}), Ce/Mn (1.7 mg g^{-1}), and Ce/Mn/Fe (1.6 mg g^{-1}) were predominantly due to the higher proportion of CeO_2 in the mixture. Thus, it was conclusive that the formation of these oxides as nanocomposites was of prime importance to improve the H_2S adsorption capacity. In our previous study, we reported H_2S adsorption over Mn_2O_3/Fe_2O_3 nanocomposite at room temperature. The study confirmed the involvement of both Mn_2O_3 and Fe_2O_3 in the oxidation of H_2S. The redox behaviour of transition metal ions in these nanocomposites was responsible for enhanced adsorption capacity.[19] Here, Ce^{3+}/Ce^{4+}, Fe^{2+}/Fe^{3+}, and Mn^{2+}/Mn^{3+} redox behaviour played an important role in the oxidation of H_2S over the nanocomposites.[33] The effect of moisture in the H_2S adsorption capacity was studied by adding moisture to the adsorbent bed, followed by the passing of H_2S gas (Fig. 6d). The presence of moisture in adsorbents negatively affected the H_2S removal process. Reportedly, moisture enhances the H_2S removal capacity of metal oxides, where the formation of moisture film on the surface promotes reactive dissociation of H_2S molecules.[34] On the contrary, moisture may decrease the adsorption capacity by competing with the H_2S adsorption sites.[8,35] Here, we expected the competitive effect of water molecules for the active sites.

The effect of bed loading was studied by varying CeMnFe mass with a fixed flow rate of 0.3 L min^{-1} (Fig. 7a). The adsorption capacity slightly improved with the increase in the bed loading due to increased contact time with the increased adsorbent mass (bed length).[36] The effect of flow rate on CeMnFe adsorption capacity was studied by varying the flow rate with a fixed adsorbent mass of 1.0 g (Fig. 7b). The adsorption capacity of 28.3 mg g^{-1} with 0.2 L min^{-1} decreased to 12.0 mg g^{-1} with 0.3 L min^{-1} flowrate. The increasing flow rate disfavored the adsorption process by decreasing the contact time, which, in turn, lowered the H_2S interaction with the CeMnFe composite. A drastic decrease in the adsorption capacity was due to a low surface area and porosity, which resulted in limited diffusion of H_2S at a higher flow rate. The competitive effect of air constituent on the H_2S adsorption process was studied by passing ambient air through the adsorbent bed for 1 h, which was followed by H_2S gas (Fig. 7c). The main components of ambient air, *i.e.* O_2, CO_2, and moisture, play a decisive role in the H_2S removal process. CO_2 is an acidic gas, which shows competitive behavior for H_2S adsorption and negatively affects the adsorption capacity.[37] While O_2 promotes the adsorption process by forming oxidized sulfur

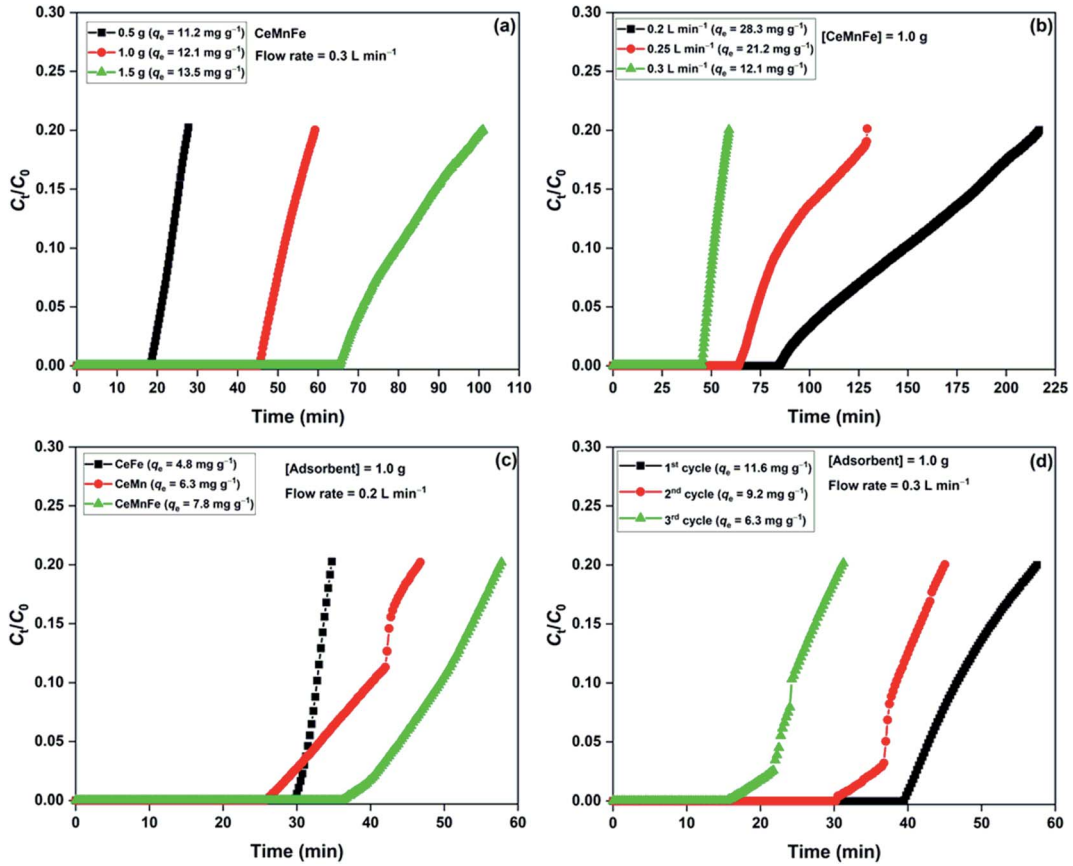

Fig. 7 (a) Effect of dosage; (b) effect of flow rate; (c) effect of ambient air on H_2S adsorption capacity; (d) reusability of CeMnFe.

byproducts, moisture lowers the H_2S adsorption capacity, observed in the present study. The decreased adsorption capacity of CeFe (4.8 mg g^{-1}), CeMn (6.3 mg g^{-1}), and CeMnFe (7.8 mg g^{-1}) showed that the negative role of CO_2 and moisture outweighs the positive role of O_2. Nonetheless, the adsorption capacity was satisfactory. The reusability of CeMnFe was tested by soaking the spent adsorbent in 0.9 mol L^{-1} ammonium hydroxide solution for 2 days (Fig. 7d). The material showed the adsorption capacity of 11.6, 9.2, and 6.3 mg g^{-1} in the first, second, and third cycle, respectively. Thus, it was possible to regenerate the synthesized nanocomposites for multiple cycles and recover H_2S-oxidized products as ammonium sulfate (liquid fertilizer).[34]

The adsorption capacity of synthesized nanocomposites was compared with the reported adsorbents in the literature. The adsorption capacity of CeMnFe was found higher than the Fe and Mn-based adsorbents (Table 2). In the literature, Ce-based adsorbents have not been reported for room temperature removal of H_2S. Thus, the study provides the first account of CeO_2-based adsorbents for H_2S removal in ambient conditions.

3.3. Adsorption mechanism

The distribution of sulfur in the spent CeMnFe nanocomposite was confirmed by EDAX elemental mapping (Fig. 8). Besides Ce, Mn, O, and Fe in the nanocomposite, wide distribution of S was observed after H_2S adsorption. The wide distribution of S in the adsorbent was an indication of the delocalized catalytic sites over oxides of Ce, Mn, and Fe. Thus, preliminary assessment from the EDAX analysis showed the involvement of all three oxides in the adsorption of H_2S. The PXRD pattern of CeMnFe before and after H_2S adsorption is shown in Fig. S5.† The diffraction patterns showed no new peaks for sulfur species. Both patterns were nearly similar, suggesting no phase transformation in the nanocomposite. Moreover, there was no shift in the diffraction peaks after H_2S adsorption, which indicated an insignificant lattice S^{2-} in the metal oxide lattice. Since vacant sites were not traced in these nanocomposites, it was an unlikely event to observe the incorporation of S^{2-} in the lattice. Other pathways involved the reactive interaction of H_2S with the metal oxide surface yielding HS^- and –OH group.[43] More information on the S species and involvement of metal ions in the process have been probed using XPS analysis.

The XPS analysis for the spent CeMnFe nanocomposite is available in Fig. 9. Apart from Ce, Mn, Fe, and O, 2.39% of S was confirmed based on the % atomic composition (Fig. 9a). The HRXPS S 2p spectrum of spent CeMnFe had a peak at 168.0 eV for SO_4^{2-} species (Fig. 9b).[7] Other than sulfate, no other species like sulfur or sulfide species could be detected by any analysis. The sulfate presence in adsorbents was confirmed by stripping the spent nanocomposites with distilled water. A 1.0 g of spent adsorbent was placed in 15 mL of distilled water and left for

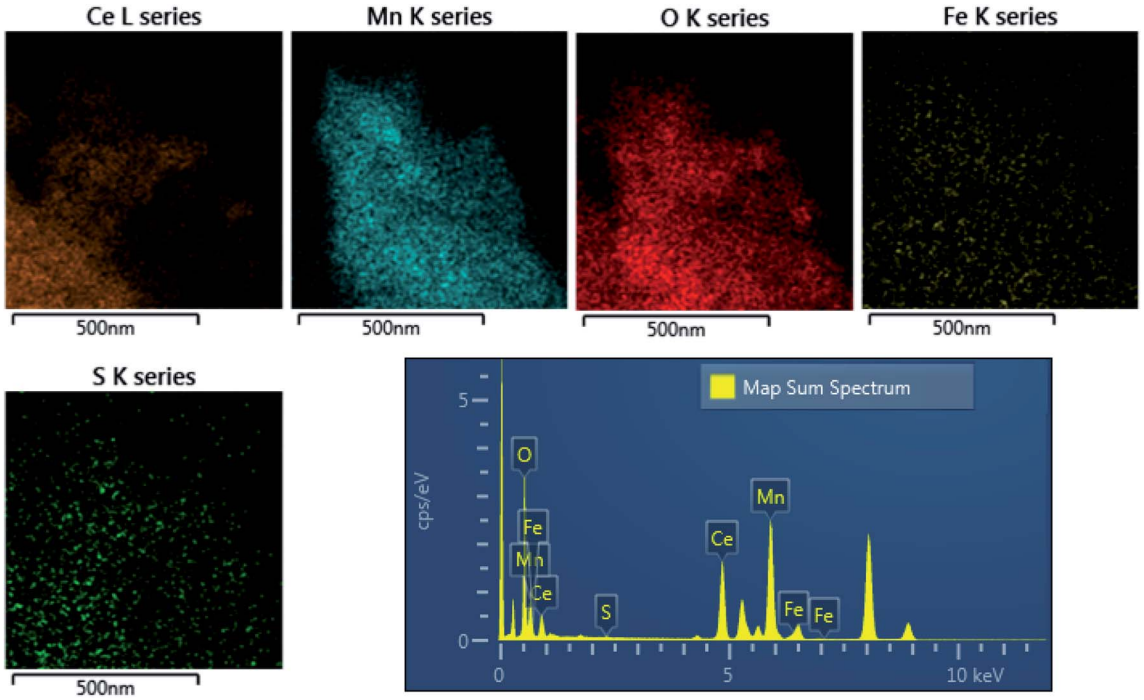

Fig. 8 TEM-EDAX analysis of H_2S-adsorbed CeMnFe.

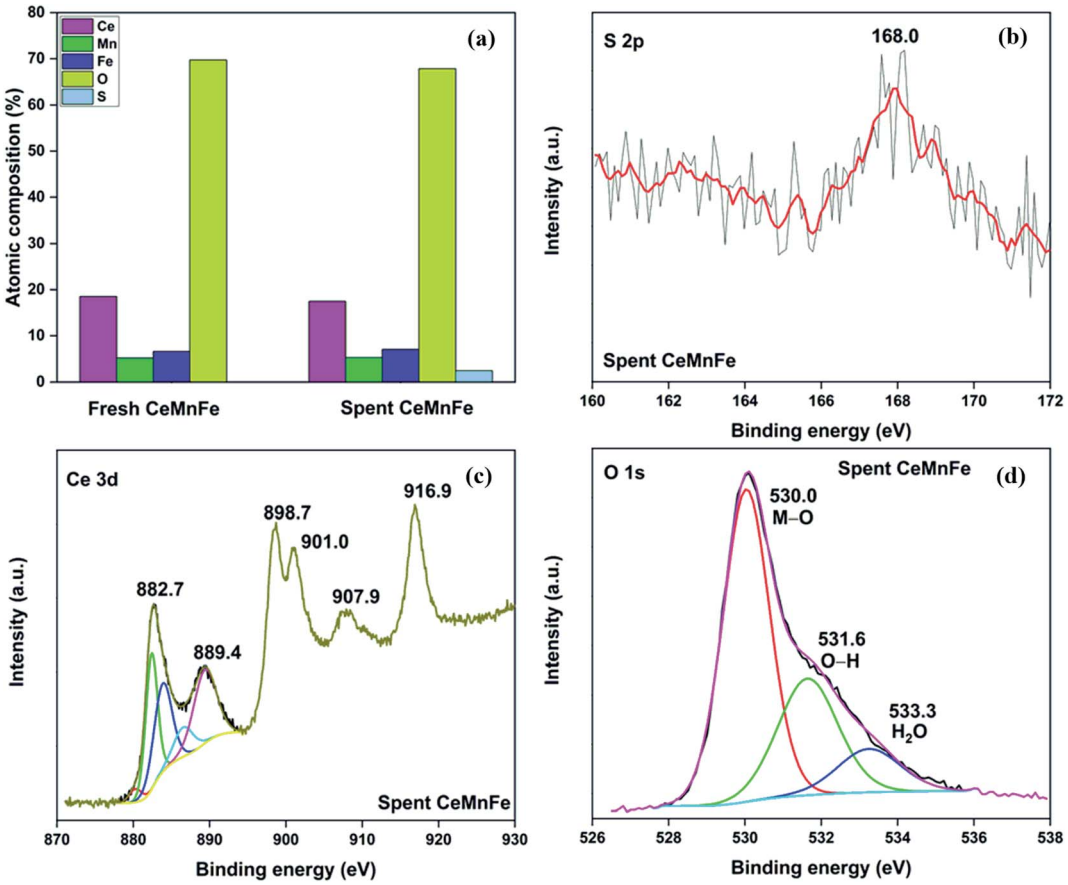

Fig. 9 (a) XPS elemental composition; HRXPS (b) S 2p; (c) Ce 3d; (d) O 1s spectra of spent CeMnFe.

48 h at room temperature. After the phase separation, the aqueous phase was analyzed by ion chromatography, which showed the presence of 0.40, 0.44, and 0.55 mg L^{-1} of SO_4^{2-} ions in CeFe, CeMn, and CeMnFe, respectively. These observations confirmed the oxidation of H_2S to sulfates over mixed metal oxide nanocomposites. The HRXPS Mn 2p spectra of spent CeMnFe showed a peak shift towards higher binding energy due to the interaction of sulfate species with the Mn sites (Fig. S6†). The weak signals of Fe 2p made it difficult to ascertain its role in the oxidation process (Fig. S7†). The HRXPS Ce 3d spectra had contributions from Ce^{3+} and Ce^{4+} sites (Fig. 9c). The $Ce^{3+}/(Ce^{3+} + Ce^{4+})$ ratio in CeMnFe dropped from 25.5% in fresh sample to 13.1% in the spent sample, which suggested the involvement of Ce^{3+}/Ce^{4+} catalytic system in the H_2S oxidation process.[43] In the HRXPS O 1s spectra, three contributions from lattice oxygen (59.9%), hydroxyl groups (28.8%), and H_2O (11.3%) (Fig. 9d). Based on the analysis, the following reactions have been proposed for the oxidation process.

$$2(O^{2-}) + H_2S \rightarrow S^{2-} + 2(-OH) \quad (2)$$

$$2M^{n+} + S^{2-} \rightarrow 2M^{(n-1)} + S \quad (3)$$

$$2M^{(n-1)+} + \frac{1}{2}O_2 \rightarrow 2M^{n+} + O^{2-} \quad (4)$$

$$S + \frac{3}{2}O_2 + H_2O \rightarrow H_2SO_4 \quad (5)$$

Since we have observed abundant hydroxyl groups and water molecules in the spent CeMnFe, these reactant species were not the reaction-driven species for the oxidation process. Eqn (4) and (5) hinted at the important role of adsorbed molecular oxygen in the $M^{(n-1)+}/M^{n+}$ catalytic system and the formation of sulfate species. Thus, the deactivation of the oxidation process was due to the consumption of molecular oxygen during the oxidation process.

4. Conclusion

We have developed a novel one-step method for the fabrication of mixed metal oxide nanocomposites of Ce/Mn/Fe. The nanocomposites were synthesized by air calcination of molten salt solutions at 700 °C. The microscopic analyses confirmed the formation of polyhedral nanoparticles of size 10–20 nm, which agglomerated to form nanospheres. The PXRD patterns confirmed CeO_2, α-Fe_2O_3, and α-Mn_2O_3 in respective nanocomposites. The synthesized nanocomposites have a surface area in the range of 16–21 $m^2\ g^{-1}$. The nanocomposites were studied for the adsorptive removal of H_2S gas in ambient conditions. CeMnFe showed a superior adsorption capacity compared to other synthesized nanocomposites. The maximum adsorption capacity of 28.3 mg g^{-1} was recorded for CeMnFe with 500 ppm of H_2S gas and 0.2 L min^{-1} of flow rate. The TEM-EDAX analysis confirmed the presence of S species over the nanocomposite. The XRD and XPS analyses proved the formation of sulfate species as the byproduct of H_2S oxidation. The study provides an easy method for the fabrication of mixed metal nanocomposites with excellent physicochemical properties. Moreover, we report the first instance of using CeO_2-based materials for the room temperature desulfurization process.

Author contributions

N. K. G. was responsible for conceptualization, data curation, formal analysis, software, writing the original draft. N. K. G and J. B. were in charge of methodology, visualization, and validation. K. S. K was responsible for funding acquisition, investigation, project administration, resources, and supervision.

Conflicts of interest

There are no conflicts to declare.

Acknowledgements

The authors are very grateful for the funds [Project #20210152-001] provided by the "Korea Institute of Civil Engineering and Building Technology" (KICT), Republic of Korea.

References

1 M. S. Shah, M. Tsapatsis and J. I. Siepmann, *Chem. Rev.*, 2017, **117**, 9755–9803.
2 L. Popoola, A. Grema, G. Latinwo, B. Gutti and A. Balogun, *Int. J. Ind. Chem.*, 2013, **4**, 35.
3 O. W. Awe, D. P. Minh, N. Lyczko, A. Nzihou and Y. Zhao, *J. Environ. Chem. Eng.*, 2017, **5**, 1809–1820.
4 S. Wang, H. Nam and H. Nam, *J. Environ. Chem. Eng.*, 2020, **8**, 103683.
5 C. N. Okonkwo, H. Fang, D. S. Sholl, J. E. Leisen and C. W. Jones, *ACS Sustainable Chem. Eng.*, 2020, **8**, 10102–10114.
6 L. H. de Oliveira, J. G. Meneguin, M. V. Pereira, E. A. da Silva, W. M. Grava, J. F. do Nascimento and P. A. Arroyo, *Microporous Mesoporous Mater.*, 2019, **284**, 247–257.
7 N. K. Gupta, S. Kim, J. Bae and K. S. Kim, *RSC Adv.*, 2021, **11**, 4890–4900.
8 N. K. Gupta, S. Kim, J. Bae and K. Soo Kim, *Chem. Eng. J.*, 2021, **411**, 128536.
9 A. Georgiadis, N. Charisiou and M. Goula, *Catalysts*, 2020, **10**, 521.
10 K. V. Bineesh, D.-K. Kim, D.-W. Kim, H.-J. Cho and D.-W. Park, *Energy Environ. Sci.*, 2010, **3**, 302.
11 A. A. Davydov, V. I. Marshneva and M. L. Shepotko, *Appl. Catal., A*, 2003, **244**, 93–100.
12 T. Montini, M. Melchionna, M. Monai and P. Fornasiero, *Chem. Rev.*, 2016, **116**, 5987–6041.
13 H. T. Bui, S. Weon, J. W. Bae, E.-J. Kim, B. Kim, Y.-Y. Ahn, K. Kim, H. Lee and W. Kim, *J. Hazard. Mater.*, 2021, **404**, 123976.
14 D.-H. Kang, M.-I. Kim and D.-W. Park, *Korean J. Chem. Eng.*, 2016, **33**, 838–843.
15 V. Palma and D. Barba, *Int. J. Hydrogen Energy*, 2014, **39**, 21524–21530.

16 D. N. Oosthuizen, D. E. Motaung and H. C. Swart, *Appl. Surf. Sci.*, 2020, **505**, 144356.
17 Z. Li, X. Niu, Z. Lin, N. Wang, H. Shen, W. Liu, K. Sun, Y. Q. Fu and Z. Wang, *J. Alloys Compd.*, 2016, **682**, 647–653.
18 M. Xue, R. Chitrakar, K. Sakane and K. Ooi, *Green Chem.*, 2003, **5**, 529–534.
19 S. Kim, N. K. Gupta, J. Bae and K. S. Kim, *J. Environ. Chem. Eng.*, 2021, **9**, 105216.
20 P. S. Murphin Kumar, S. Thiripuranthagan, T. Imai, G. Kumar, A. Pugazhendhi, S. R. Vijayan, R. Esparza, H. Abe and S. K. Krishnan, *ACS Sustainable Chem. Eng.*, 2017, **5**, 11290–11299.
21 N. K. Gupta, Y. Ghaffari, J. Bae and K. S. Kim, *J. Mol. Liq.*, 2020, **301**, 112473.
22 J. Wang, G. Zhu, L. Deng, L. Kang, Z. Hao and Z. Liu, *CrystEngComm*, 2012, **14**, 8253.
23 M. S. Pujar, S. M. Hunagund, D. A. Barretto, V. R. Desai, S. Patil, S. K. Vootla and A. H. Sidarai, *Bull. Mater. Sci.*, 2020, **43**, 24.
24 P. Pal, A. K. Giri, S. Mahanty and A. B. Panda, *CrystEngComm*, 2014, **16**, 10560–10568.
25 G. Bharath and N. Ponpandian, *RSC Adv.*, 2015, **5**, 84685–84693.
26 Y. H. Leung, M. M. N. Yung, A. M. C. Ng, A. P. Y. Ma, S. W. Y. Wong, C. M. N. Chan, Y. H. Ng, A. B. Djurišić, M. Guo, M. T. Wong, F. C. C. Leung, W. K. Chan, K. M. Y. Leung and H. K. Lee, *J. Photochem. Photobiol., B*, 2015, **145**, 48–59.
27 S. Gnanam and V. Rajendran, *J. Sol-Gel Sci. Technol.*, 2011, **58**, 62–69.
28 S. Bellayer, L. Viau, Z. Tebby, T. Toupance, J. L. Bideau and A. Vioux, *Dalton Trans.*, 2009, 1307.
29 S. Poulin, R. França, L. Moreau-Bélanger and E. Sacher, *J. Phys. Chem. C*, 2010, **114**, 10711–10718.
30 J. Pang, W. Li, Z. Cao, J. Xu, X. Li and X. Zhang, *Appl. Surf. Sci.*, 2018, **439**, 420–429.
31 M. C. Biesinger, L. W. M. Lau, A. R. Gerson, R. St and C. Smart, *Appl. Surf. Sci.*, 2010, **257**, 887–898.
32 Y.-H. Son, P. T. M. Bui, H.-R. Lee, M. S. Akhtar, D. K. Shah and O.-B. Yang, *Coatings*, 2019, **9**, 631.
33 A. Mirzaei, S. S. Kim and H. W. Kim, *J. Hazard. Mater.*, 2018, **357**, 314–331.
34 N. K. Gupta, J. Bae and K. S. Kim, *Chem. Eng. J.*, 2021, 130909.
35 C. Weinlaender, R. Neubauer, M. Hauth and C. Hochenauer, *Chem. Ing. Tech.*, 2017, **89**, 1247–1254.
36 N. Q. Long and T. X. Loc, *Adsorption*, 2016, **22**, 397–408.
37 R. Sitthikhankaew, D. Chadwick, S. Assabumrungrat and N. Laosiripojana, *Fuel Process. Technol.*, 2014, **124**, 249–257.
38 D. M. Cristiano, R. de A. Mohedano, W. C. Nadaleti, A. B. de Castilhos Junior, V. A. Lourenço, D. F. H. Gonçalves and P. B. Filho, *Renewable Energy*, 2020, **154**, 151–160.
39 C. Costa, M. Cornacchia, M. Pagliero, B. Fabiano, M. Vocciante and A. P. Reverberi, *Materials*, 2020, **13**, 4725.
40 Y. Cao, X. Zheng, Z. Du, L. Shen, Y. Zheng, C. Au and L. Jiang, *Ind. Eng. Chem. Res.*, 2019, **58**, 19353–19360.
41 S. Rezaei, A. Tavana, J. A. Sawada, L. Wu, A. S. M. Junaid and S. M. Kuznicki, *Ind. Eng. Chem. Res.*, 2012, **51**, 12430–12434.
42 D. Nguyen-Thanh, K. Block and T. J. Bandosz, *Chemosphere*, 2005, **59**, 343–353.
43 X. Zheng, Y. Li, L. Zhang, L. Shen, Y. Xiao, Y. Zhang, C. Au and L. Jiang, *Appl. Catal., B*, 2019, **252**, 98–110.